SUPPLEMENTARY INFORMATION

Supplementary Discussion for:

An Asteroid Breakup 160 My Ago as the Probable Source of the K-T Impactor

W. F. Bottke, D. Vokrouhlický, and D. Nesvorný

July 6, 2007

1 Identifying the Baptistina Family

1.1 Methods of family detection

To identify members of the BAF, we applied the Hierarchical Clustering Method (HCM) to search for asteroids near (298) Baptistina in proper element space (e.g., Bendjoya and Zappalà 2002, and references therein). Proper orbital elements, being more constant over time than instantaneous orbital elements (Knežević et al. 2002), provide a dynamical criterion of whether or not a group of bodies has a common ancestor. The orbital parameters of (298) Baptistina are proper semimajor axis $a_{\rm P} = 2.264$ AU, proper eccentricity $e_{\rm P} = 0.15$, and proper inclination $i_{\rm P} = 5.7^\circ$ (Knežević and Milani 2003).

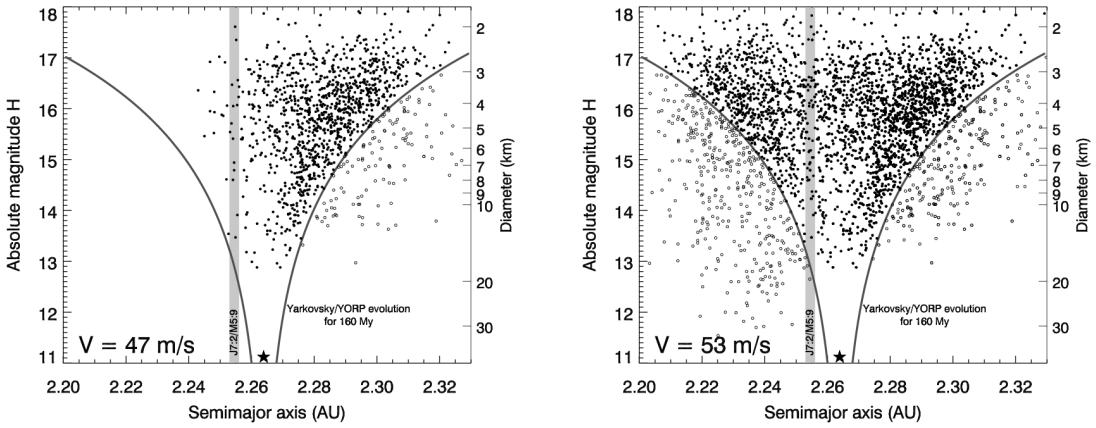

Figure S1: The BAF projected onto a plane of proper semimajor axis a vs. absolute magnitude H. On the right ordinate, we show asteroid diameters for a typical C-type asteroid albedo of 0.04. The central and largest body of the family, C-type asteroid (298) Baptistina, has proper semimajor axis $a = 2.264$ AU (the black star). The BAF was identified using the Hierarchical Clustering Method (HCM) that locates bodies in the neighborhood of (298) Baptistina's orbit in proper element space with mutual velocities less than a threshold limit $V_{\rm cutoff}$. On the left, we see 1199 linked objects with $V_{\rm cutoff} = 47$ m s^{-1}. On the right, we see 3042 linked objects with $V_{\rm cutoff} = 53$ m s^{-1}. The right plot shows our preferred definition of the Baptistina family. The family's age (see Sec. 3) was used to estimate its maximal extension in (a, H) (shown as dark gray curves). The objects shown as open circles are assumed to be mostly interlopers.

The HCM starts with an individual asteroid orbit defined in proper elements and identifies bodies in its neighborhood with mutual distances less than a threshold velocity limit ($V_{\rm cutoff}$). We defined the distance in $(a_{\rm P}, e_{\rm P}, i_{\rm P})$ space by:

$$V = n a_{\rm P} \sqrt{C_a(\delta a_{\rm P}/a_{\rm P})^2 + C_e(\delta e_{\rm P})^2 + C_i(\delta \sin i_{\rm P})^2} \ , \qquad (1)$$

where $n a_{\rm P}$ is the heliocentric velocity of an asteroid on a circular orbit having semimajor axis $a_{\rm P}$. We also define $\delta a_{\rm P} = |a_{\rm P}^{(1)} - a_{\rm P}^{(2)}|$, $\delta e_{\rm P} = |e_{\rm P}^{(1)} - e_{\rm P}^{(2)}|$, and $\delta \sin i_{\rm P} = |\sin i_{\rm P}^{(1)} - \sin i_{\rm P}^{(2)}|$. The indices (1) and

(2) denote the two bodies in consideration. The values C_a, C_e, and C_i are constants; we use $C_a = 5/4$, $C_e = 2$, and $C_i = 2$ (see Zappalà et al. 1990). Other choices for these constants can be found in the literature, but we find they yield similar results.

The output of HCM is a cluster of asteroids with member bodies connected by a chain in (a_P, e_P, i_P) space with the length of each link $\leq V_{\rm cutoff}$ (see Fig. S1). To identify members of the BAF, we tested $V_{\rm cutoff}$ values between 40-60 m s^{-1}. With $V_{\rm cutoff} > 55$ m s^{-1}, the algorithm starts to connect background bodies that, by eye, are unlikely to be members of the BAF. With $V_{\rm cutoff} < 52$ m s^{-1}, the algorithm fails to connect to the left side of the family, mainly because it has been depleted near the J7:2/M5:9 (see Fig. S1). After several tests, we decided to adopt $V_{\rm cutoff} = 53$ m s^{-1} to define the BAF, though this does allow the inclusion of more interlopers than lower velocity cases.

1.2 The Orbital Location of the Baptistina Family

Using the results from Sec. 1.1, we can plot the orbital location of the Baptistina asteroid family (BAF) within the inner main belt (Fig. S2). The Flora family is located to the immediate left of Baptistina, while the Vesta family is the cluster of asteroids with proper inclinations 6°-7°.

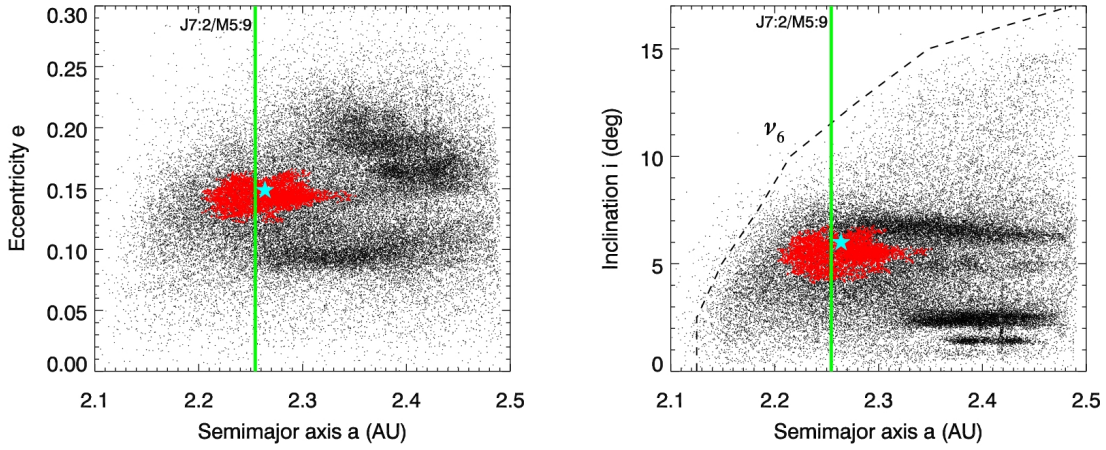

Figure S2: The location of the Baptistina family in proper semimajor axis a, eccentricity e, and inclination i space. The red dots show the Baptistina family for 3042 objects with $V_{\rm cutoff} = 53$ m s^{-1} (see Sec. 1). The largest body of the family, C-type asteroid (298) Baptistina, has proper semimajor axis $a = 2.264$ AU, $e = 0.15$, and $i = 5.7°$ (blue star). The black dots show the numbered asteroids of the main asteroid belt for $H < 17$. The green line corresponds the chaotic region produced by the adjacent 7:2 mean motion resonance with Jupiter (J7:2) and the 5:9 mean motion resonance with Mars (M5:9). The dashed line in the (a, i) plot is the approximate position of the ν_6 secular resonance.

The BAF is nearly cut in half by two adjacent resonances: the 7:2 mean motion resonance with Jupiter (J7:2) at $a = 2.2559$-2.2569 AU and the 5:9 mean motion resonance with Mars (M5:9) located at 2.2542-2.2550 AU (Morbidelli and Nesvorný 1999) (Figs. S1, S2). Together, these resonances are reasonably efficient at pushing objects out of the main belt. Moreover, the position of the J7:2/M5:9 resonances near the center of the BAF means that slow-moving $D > 5$ km objects do not have to drift very far by the Yarkovsky effect to enter into it. This makes the BAF particularly well suited to affect the terrestrial planet impact flux.

An examination of the innermost main belt region shows two other prominent families capable of producing meaningful showers: Flora (2.2 AU; estimated age of 0.47 Ga; see main text) and Vesta (2.36 AU; estimated age unknown but probably $\sim$ 1-3.5 Ga; Bogard 1995; Marzari et al. 1996; Carruba et al. 2005). Because they are significantly older than the BAF (160 Ma, see main text and Sec. 3), any surge of impactors produced by the Flora and Vesta family-forming events should now be over. Nevertheless, both families continue to provide significant numbers of objects to the terrestrial planet region via collisional cascades coupled with Yarkovsky/YORP evolution; we believe it likely that the

Flora and Vesta families are the primary sources of the L-chondrites and Howardite-Eucrite-Diogenite (HED) meteorites, respectively (e.g., Burbine et al. 2002; Bottke et al. 2005; Nesvorný et al. 2007).

2 The Taxonomy and Colors of the Baptistina Family

There is limited information on the spectral properties of BAF members at present. Using an HCM cutoff limit of $V_{\rm cutoff} = 57.5$ m s^{-1} rather than our preferred value of 53 m s^{-1}, Mothé-Diniz et al. (2005) described the taxonomic classification of 8 BAF members based on their spectral features over visible wavelengths (Xc, C, L, S, S, V, A, and X). Tests by our group, however, indicate most of these objects are BAF interlopers. Two that are not, (298) Baptistina and (2093) Genichesk, have Xc and C-type taxonomic classifications, respectively, according to the SMASSII scheme (Bus et al. 2002). For reference, the Xc class fits within the E, M, and P classes described by the Tholen and Howell taxonomic classification schemes (see Bus et al. 2002).

Fig. S3 summarizes what is known about the colors of the Baptistina family from the Sloan Digital Sky Survey (SDSS) (Ivezić et al. 2001). See Nesvorný et al. (2005) for additional details.

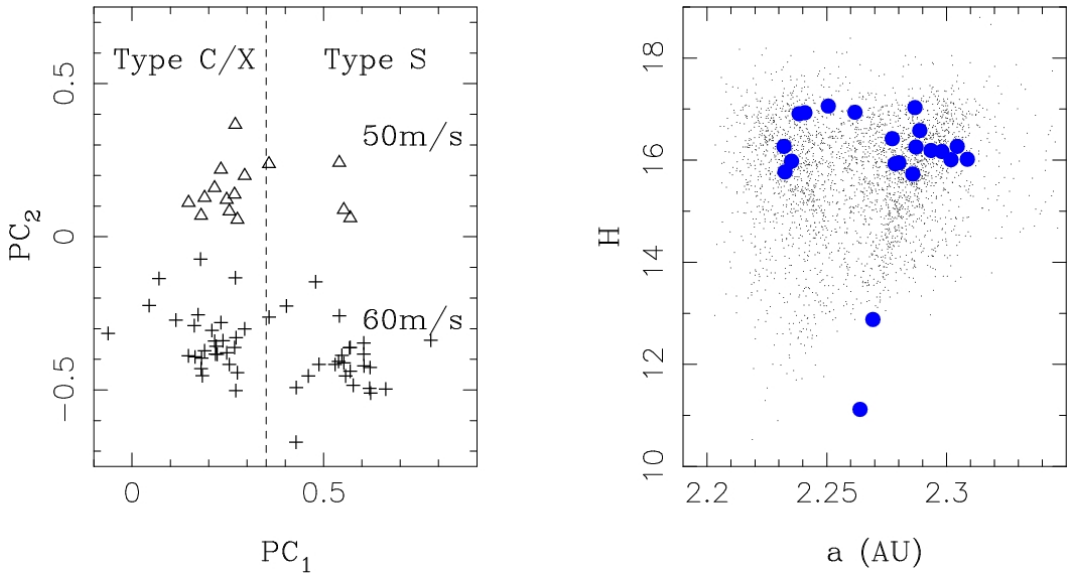

Figure S3: The colors of the Baptistina family from the Sloan Digital Sky Survey (SDSS). The left side shows shows principal color components PC_1 and PC_2 defined by the SDSS. For convenience, we have plotted two choices for $V_{\rm cutoff}$ on the same plot; 50 and 60 m s^{-1}. They are shown with different symbols, with the 60 m s^{-1} objects offset by 0.5 in the $-y$ direction to make it easier to compare the two sets. The right side shows the semimajor axis a and absolute magnitude H for the known members of the BAF defined at 53 m s^{-1}. The vertical dashed line shows separation in PC_1 between the taxonomic complexes C/X and S. The blue dots show BAF members that have been detected by the SDSS. All of these objects have C/X-complex colors, consistent with a genetic link to (298) Baptistina. The reader should also be aware of two additional issues that affect the interpretation of these plots: (i) the SDSS data release used here (ADR3) is several times more efficient at detecting $H \approx 16$ objects than $H \approx 14$ objects and (ii) the reported H values of many BAF objects may be systematically too dim; see Sec. 4 for additional details.

For this figure, we defined members of the Baptistina family at two different cutoffs, $V_{\rm cutoff} = 50$ m s^{-1} and 60 m s^{-1} and plotted their SDSS color components (PC_2 is offset for clarity). At 60 m s^{-1}, the sample shows a roughly equal mix of C/X and S asteroids. At 50 m s^{-1}, however, the C/X type asteroids dominate, clearly indicating that the BAF has C/X-complex colors. We infer that the preferred cutoff value for the Baptistina family is ≈ 50 m s^{-1}.

The right panel shows the semimajor axis a and absolute magnitude H for the known members of the BAF defined at 53 m s^{-1}. Note that the distribution has the two-lobed, V-shaped form characteristic of asteroid families dispersed by the Yarkovsky effect (Vokrouhlický et al. 2006a). The blue circles show members that have been detected by the SDSS that have C/X-complex colors. These results are consistent with the Xc and C-type taxonomic classifications of (298) Baptistina and (2093) Genichesk, respectively.

There are several reasons why so many S-type and/or other high albedo interlopers are found for $V_{\rm cutoff} = 60$ m s^{-1}. First, the BAF is located in the middle of dense population of background objects, many which come from the nearby S-type Flora or V-type Vesta families. Second, the size frequency distributions (SFDs) of the BAF and background populations are very different from one another. The SFD for large BAF members consists of one large object, a gap, and then numerous smaller objects (see Fig. 2 of main text), while the background SFD in the same diameter range has many intermediate-sized objects and thus is more continuous. Finally, the conversion of these SFDs to a single H distribution overwhelmingly favors high albedo S- or V-type asteroids over low albedo C/X-complex asteroids. Recall that for a given H value, S- and V-type asteroids are typically several times smaller (and, all things being equal, more numerous) than C/X-complex asteroids (see Eq. 8 in Sec. 4). Together, these effects mean that spectroscopic surveys like SMASSII and S3OS2, which tend to detect the brightest main belt objects, are generally biased toward BAF interlopers. We believe these biases may be particularly acute for $H < 13.5$ objects in the BAF; as shown in Fig. S1, the number density of these objects for $V_{\rm cutoff} = 53$ m s^{-1} is roughly the same as the background population.

The reverse is true, however, when asteroid colors from the SDSS are used. Because the SDSS can detect dimmer asteroids than SMASS or S3OS2 (see Fig. S3 caption), it is more sensitive to the steeper portions of the BAF's SFD where it dominates the background SFD. Fig. S3 shows that SDSS objects near the BAF predominantly have C/X-complex colors. This numerical superiority occurs despite the fact that, for a given H value, C/X objects are larger than the S- or V-type objects that dominate the background. We conclude from this that the Baptistina parent body was a dark, primitive asteroid that produced fragments with C- to X-type spectra. We predict that interlopers make up 10-20% of the overall BAF as a function of H, with this value varying somewhat from low H values to high ones. For shorthand reasons, we refer to the BAF in our paper as a C-type or C-complex family.

Finally, we do not yet fully understand why the spectral properties in the BAF appear to range from C-types to Xc-types. It is possible this may have to do with where the fragments were originally located in the $D \approx 170$ km parent body. Note that the interior of the Baptistina parent body almost certainly experienced varying degrees of heating and aqueous alteration at depth. If so, BAF members with other taxonomic types within the C/X-complex may be found in the future.

3 Determining the Age of the Baptistina Family

3.1 Introduction

The ages of asteroid families can only be computed in certain circumstances. The most precise method is a direct backward integration of the family members. This works for extremely young families (< 10 My old) like Datura (e.g. Nesvorný et al. 2006, Nesvorný and Vokrouhlický 2006), Karin (e.g. Nesvorný et al. 2002) or Veritas (e.g. Nesvorný et al. 2003). For families older than this threshold, however, the influence of planetary perturbations, chaos, and Yarkovsky/YORP-driven evolution on individual family members compels us to use alternative age determination models.

One such method developed by Vokrouhlický et al. (2006a) is applicable to several families that are ≤ 1 Gy old (see also Sec. 3.5 and Vokrouhlický et al. 2006b,c). It assumes that families dynamically evolve in the following manner. After a catastrophic collision produces an asteroid family, the family members spread in semimajor axis a, moving inward toward and outward away from the Sun by the Yarkovsky effect (Bottke et al. 2002a, 2006b). Simultaneously, YORP torques tilt the orientation of each asteroid's spin axis toward obliquities of 0° or 180° (e.g., Čapek and Vokrouhlický 2004) where Yarkovsky da/dt rates are highest. Over time, these mechanisms clear out the family center and preferentially push material toward extreme a values. The result can be seen in Fig. 1 of the main text, where $D = 2$-5 km diameter members of the Baptistina asteroid family (BAF) reside in an (a, H) distribution characterized by two asteroid clouds divided by a depleted center (see also Sec. 3.5 for additional examples).

Vokrouhlický et al. (2006a) found that by using what we know of Yarkovsky/YORP evolution, we could take advantage of this characteristic shape in (a, H) to estimate the family's age. The model and its application to the BAF is shown below.

3.2 A new representation of the Baptistina family

The goal of the Vokrouhlický et al. (2006a) method is to reproduce the unique (a, H) distribution seen in Fig. S1 of the Supplemental Discussion. Instead of directly working in this 2-D space, however, Vokrouhlický et al. (2006a) constructed a 1-D representation of the same information. This was done by defining a curvilinear coordinate C in the (a, H) plane using

$$0.2\,H = \log \left| \frac{\Delta a}{C} \right| , \tag{2}$$

with $\Delta a = a - a_{\rm c}$. Here $a_{\rm c}$ is the center of the family. For the BAF, we define it as the proper semimajor axis of (298) Baptistina ($a_{\rm c} = 2.2638$ AU). Eq. (2) allows us to partition the (a, H) plane into intervals $(C, C + \Delta C)$, with $C = 0$ at the center of the family and large $|C|$ values away from the center. Choosing $\Delta C = 1.5 \times 10^{-6}$ AU, we can represent the distribution of asteroids in the family by $N_{\rm obs}(C)$, defined as the number of bodies in the bin $(C, C + \Delta C)$.

Given that the BAF is located in a dense, complicated portion of the main belt (see Secs. 1 and 2), it was important to eliminate as many interlopers as possible without affecting the family's (a, H) structure. After some trial-and-error, we decided to apply our age determination model to a more conservative identification of the BAF, namely $V_{\rm cutoff} = 47$ m s^{-1} (Fig. S1, left panel). This limits us to Baptistina members from the right lobe of the family ($a \geq a_{\rm c}$; $C \geq 0$); the left lobe is not detected until $V_{\rm cutoff} = 53$ m s^{-1} (Fig. S1, right panel) because the J7:2/M5:9 has depleted asteroids with $a \leq a_{\rm c}$.

The distribution $N_{\rm obs}(C)$ of BAF members is shown in the top left corner of Fig. S4. The observed central depletion of small BAF members reflects the minimum $N_{\rm obs}(C)$ value for $C = 0$. The maximum density of small BAF members in the (a, H) plane, displaced from $a_{\rm c}$, translates into the maximum $N_{\rm obs}(C)$ value for $C \simeq 1.5 \times 10^{-5}$ AU.

3.3 Age determination procedure

Taking this data, we used the Monte Carlo code described in Vokrouhlický et al. (2006a) to determine the input parameters needed to match the $N_{\rm obs}(C)$ distribution as accurately as possible. We outline the major components of this code below:

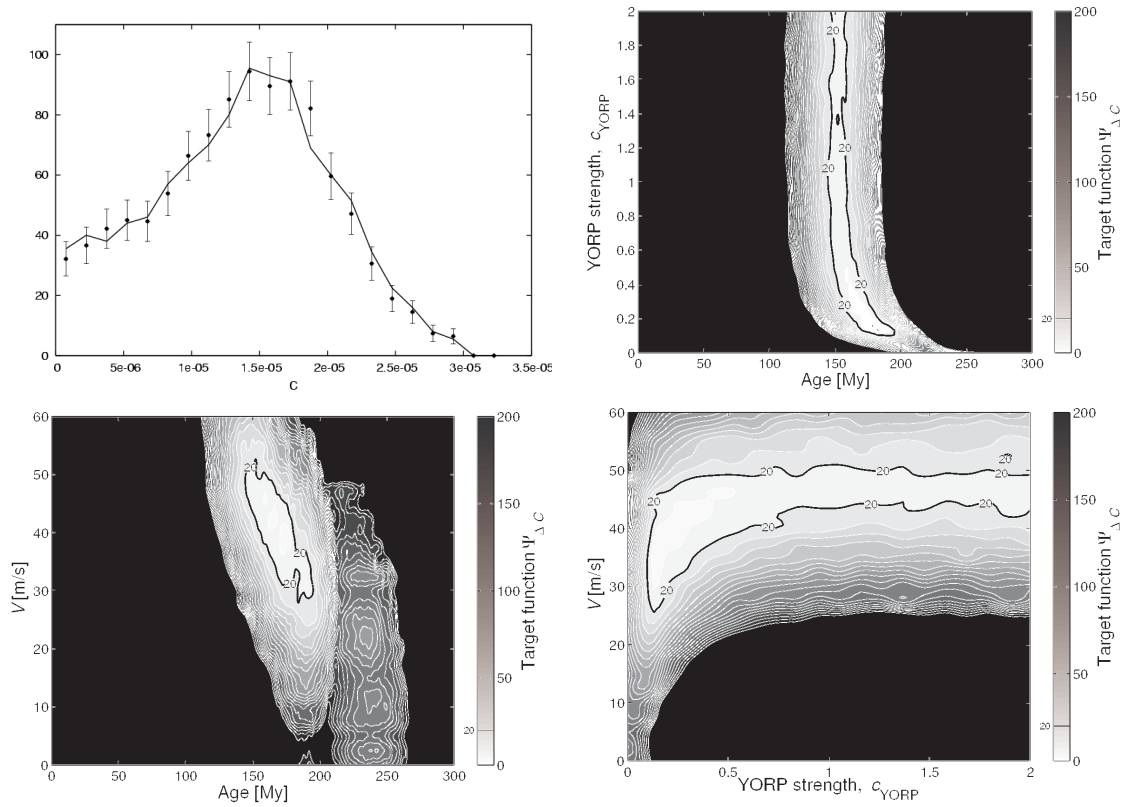

Figure S4: Results of our reconstruction of the BAF using the method of Vokrouhlický et al. (2006a), mean albedo $p_V = 0.05$, and surface thermal conductivity $K = 0.03$ W/m/K. The top left figure is the best-fit simulation $N(C)$ (solid line) compared to the observed family $N_{\rm obs}(C)$ (symbols and error-bars). The top right, bottom left, and bottom right figures show projections of the best value of the target function $\Psi_{\Delta C}$ for various pairs of solved-for parameters: (i) age T vs. YORP strength parameter $c_{\rm YORP}$, (ii) age T vs. characteristic velocity V_0 of initial ejection of $D = 5$ km fragments, and (iii) $c_{\rm YORP}$ vs. V_0. The critical-level contour $\Psi_{\Delta C} = 20$, that is used to estimate the uncertainties of our solved-for parameters, is shown in bold; contours for other values (incremented by a value of 5) of the target function are shown in light.

- The initial orbits of the BAF's fragments in proper element space were based on a test velocity distribution. The velocity components V_R, V_T and V_N along the radial, transverse, and normal directions with respect to the parent body's orbit were given the same Gaussian distribution with standard deviation $V_{\rm SD}$. We assumed $V_{\rm SD} = V_0\,(5\,{\rm km}/D)$, where V_0 is a free parameter of the model (typical values are believed to be several tens of m/s) and $V_{\rm SD}$ was thus inversely proportional to size D. This relation was derived using data from the 5.8 My old Karin family (Nesvorný et al. 2002). The fragments were set to same numbers and H values as that in BAF. The absolute magnitude H was converted to diameter D using standard methods and a constant geometric albedo of p_V. We tested various values of p_V, but settled on $p_V = 0.05$ rather than $p_V = 0.04$ (as used in the text) to account for the fact that the smaller family members may have higher albedos than the larger ones. Observations indicate that albedos tend to increase for $D < 10$ km objects (Tedesco et al. 2002).

- Apart from the size and the initial orbital elements of each fragment (a in particular), we also assigned an initial obliquity value ϵ and angular rotation velocity ω. The initial orientation of each asteroid's spin axis was assumed to be random in space, allowing $\cos\epsilon$ to be uniformly distributed in the interval $(-1, 1)$. We assumed that ω had a Gaussian distribution peaked at $\simeq 6$ hr. Values smaller than 2 hr and longer than 12 hr were rejected.

- The orbital evolution of each fragment was tracked individually, with Yarkovsky drift (e.g. Vokrouh-

lický 1998; 1999)

$$\frac{da}{dt} = \kappa_1 \cos\epsilon + \kappa_2 \sin^2\epsilon \ , \tag{3}$$

where κ_1 and κ_2 are functions depending on surface thermal parameters and the fragment's size. We used the following thermal parameters: thermal conductivity $K = 0.005 - 0.05$ W/m/K, specific heat capacity $C_p = 680$ J/kg/K, surface and bulk densities $\rho = 1.3$ g/cm^3.

- The two rotation state parameters, obliquity ϵ and rotation rate ω, undergo evolution due to the YORP effect according to:

$$\frac{d\omega}{dt} = f(\epsilon) \ , \tag{4}$$

$$\frac{d\epsilon}{dt} = \frac{g(\epsilon)}{\omega} \tag{5}$$

(e.g. Vokrouhlický and Čapek 2002, Čapek and Vokrouhlický 2004). The f- and g-functions here are the median strength of the YORP torques derived by Čapek and Vokrouhlický (2004) for asteroids with surface thermal conductivity values within the range stated above. We caution, however, that our YORP model is less certain than our Yarkovsky effect model. For this reason, we introduce a free parameter $c_{\rm YORP}$ that controls the strength of the YORP effect. We multiply this factor by the $f-$ and $g-$functions in Eqs. (4) and (5).

- Finally, we assume that non-catastrophic collisions can reorient the spin vectors of our test asteroids, which in turn affects the Yarkovsky and YORP effects. Disruptive collisions are neglected. To implement this, we follow the approach developed by Farinella et al. (1998), who obtained the following formula for the typical re-orientation timescale:

$$\tau_{\rm reor} = B\,(\omega/\omega_1)^{\beta_1}(D/D_1)^{\beta_2} \ , \tag{6}$$

with $B = 84.5$ ky, $\beta_1 = 5/6$ and $\beta_2 = 4/3$, and the reference size $D_1 = 2$ m and rotation frequency ω_1 corresponding to the rotation period of 5 hr. Propagating the family's evolution over timesteps Δt (we typically take $\Delta t \sim 500$ y), we compute at each timestep the probability $\sim \Delta t/\tau_{\rm reor}$ that the spin vector would be reset by a collision event to different (random) state.

Using the initial configuration of the BAF described above, we ran our code for a time T, typically ranging from $0 - 300$ My, and let the family evolve by the Yarkovsky/YORP effects. As mentioned above, apart from T, we consider 2 free-to-fit parameters: V_0 and $c_{\rm YORP}$. To obtain a measure of a quantitative agreement between the simulated $N(C)$ and the observed family $N_{\rm obs}(C)$, we define a pseudo-χ^2 target function

$$\Psi_{\Delta C} = \sum_{\Delta C} \frac{\left[N\,(C) - N_{\rm obs}\,(C)\right]^2}{N_{\rm obs}(C)} \ , \tag{7}$$

where formally the error assigned to the number $N_{\rm obs}(C)$ in a given bin $(C, C + \Delta C)$ is $\sqrt{N_{\rm obs}(C)}$. Summation in (7) is performed over all bins ΔC with a nonzero number $N_{\rm obs}(C)$ of residing BAF members. Our procedure seeks to minimize $\Psi_{\Delta C}$ via variations of the 3 parameters over our chosen interval of values. Admissible solutions are characterized by $\Psi_{\Delta C}$ of the order equal to the number of used bins in C (in our case we use 20), while solutions giving much larger $\Psi_{\Delta C}$ are incompatible with the observed family.

3.4 Results

Fig. S4 shows results for $p_V = 0.05$ and the surface thermal conductivity $K = 0.03$ W/m/K (corresponding well to the observed values of the thermal inertia of multi-km near-Earth asteroids by Delbó et al. 2007). The best-fit solutions are $T = 160^{+30}_{-20}$ My and $V_0 = 40 \pm 10$ m/s. The value of $c_{\rm YORP}$ is more poorly constrained. Our best-fit value of V_0 indicates that $D \sim$ 2-3 km fragments were initially ejected at ~ 73 m/s; comparable to the escape velocity expected for the $D \sim 170$ km BAF parent body (see main text). Note that tests using $V_{\rm cutoff} = 48$-50 m s^{-1} to identify the BAF yield comparable ages to those described above.

While small variations of K do not significantly modify our results (i.e., smaller values produce slightly younger family ages), smaller or larger values of p_V produce larger or smaller values of T. Vokrouhlický et al. (2006a) determined that an approximate scaling relation for this effect is $T \propto p_V^{-1/2}$. This factor can be readily applied once the true albedo is known for (298) Baptistina and numerous members of the BAF. The age of the family is also proportional to the bulk density ($T \propto \rho$), such that higher densities for BAF members lead to longer ages.

3.5 Additional Examples

For reference, Fig. S5 shows several examples of young asteroid families whose ages and initial velocity distributions have been computed by the method above (Vokrouhlický et al. 2006a). As in the case of the BAF, their shapes in (a, H) space are diagnostic of families undergoing dynamical evolution from Yarkovsky forces and spin vector evolution from YORP torques.

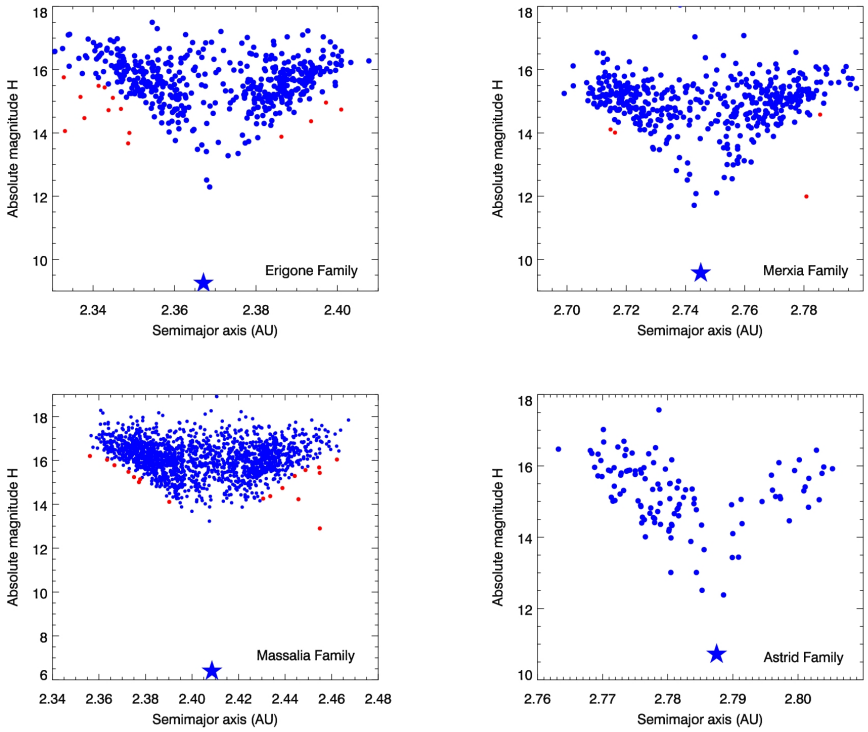

Figure S5: Additional examples of young families whose ages can be computed by our method: Erigone, Merxia, Massalia, and Astrid (see also Vokrouhlický et al. 2006a). The blue dots are the family members, the red dots are interlopers, and the blue star is the family's largest remnant. Like the BAF, these families show a two-lobed structure, evacuated center, and general "V"-shape. We find that Erigone and Merxia were produced by large catastrophic disruption events (i.e., parent body diameter $D \sim 100$ km) that occurred approximately 280 and 330 Myr ago, respectively. The Massalia family was likely produced by a cratering event on asteroid (20) Massalia less than 200 Myr ago. Finally, the Astrid family, which was produced by the disruption of a 60-70 km asteroid, is 100-200 Myr old, though there is considerable uncertainty in this result. We estimate that the initial ejection velocities for these families were only a few tens of meters per second, consistent with results from numerical hydrocode simulations of asteroid impacts.

4 Computing the Initial Number of Kilometer-Sized Asteroids in the Baptistina Family

This section describes our procedure for estimating the number of diameter $D > 1$ km asteroids that initially existed in the BAF.

We start with some essentials. Absolute magnitude H refers to the magnitude of an asteroid at zero phase angle and at unit heliocentric and geocentric distances. It allows the overall brightnesses of objects to be compared to one another without regard to distance. The Minor Planet Center (MPC) and Asteroid-Dynamics Site (AstDyS; http://newton.dm.unipi.it/) compute H values for asteroids from observational and astrometric data reported both by various asteroid surveys (e.g., Spacewatch, LINEAR, Catalina Sky Survey, LONEOS, NEAT, etc.) and individual observers. Their asteroidal H values can then be turned into D values using the equation:

$$D(\mathrm{km}) = \frac{1329}{\sqrt{p_V}} 10^{-H/5}. \tag{8}$$

with p_V defined as the visual geometric albedo (e.g., Fowler and Chillemi 1992; Pravec and Harris 2007).

Our method to get the number of $D > 1$ km bodies in the BAF is as follows:

Step 1. We gathered H values for BAF members using the databases described above. Note that the accuracy of these values depends on the magnitudes and photometry reported by various asteroid surveys. Unfortunately, the existing H catalog at the MPC appears to contain systematic errors that skew the objects toward dimmer values (see Jedicke et al. 2002). If true, these systematic errors most likely stem from a transformation used by the LINEAR survey which assumes solar color for a detected asteroid in transforming from the spectral band of observation to the B band scale that they report. Solar color corresponds to $B - V = 0.62$. In computing H magnitudes, the MPC (and others) use $B - V = 0.8$, which is a typical mean for actual asteroid colors, to convert them back to V magnitudes (A. Harris, personal communication). Additional complications include those listed by Stuart (2006), who suggested that LINEAR's poor photometric calibration over the last several years may be a byproduct of their use of the USNO A2.0 star catalog. To compensate for these potential problems, Gareth Williams at the MPC computed new H magnitudes and observational errors for our computed BAF members. These values were then compared with H values from the AstDyS database. While not identical, both sets of H values tend to yield comparable results for the computations given below.

Step 2. Following the procedure described in the main text, we found all of the BAF members with $a > a_{\mathrm{bap}}$; they were assumed to be a mirror image of those with $a < a_{\mathrm{bap}}$ ($a_{\mathrm{bap}} = 2.2638$ AU). We then doubled this population, such that the new H distribution for the BAF was comprised of (298) Baptistina and twice the H distribution with $a > a_{\mathrm{bap}}$.

Step 3. A Monte Carlo code was created to properly account for observational errors in H. Taking the BAF H values described above, we created 10,000 new sets of H values by generating sets of normally-distributed (Gaussian) random numbers, multiplying these numbers by the observational errors associated with each H value, and then adding the product to our nominal H values. The mean and standard deviation of these distributions were computed and examined for trends. Differential H distributions between $H_1 = 13.8$-14.0 and $H_2 = 15.0$-15.3 were found to be smooth, such that power laws fits to this data yielded very low χ^2 error values. Objects with $H > 15.3$ were not included in our analysis for two reasons: (i) the inner main belt may only be observationally complete for objects with $H < 15$-15.3 (Jedicke et al. 2002) and (ii) we were concerned that collisional evolution within the BAF over the last 160 My may have affected the $H > 15.3$ distribution (see Fig. 3 of main text).

Step 4. We fit log-linear curves to each of the 10,000 H distributions described above for H values between $H_1 = 13.8$-14.0 and $H_2 = 15.0$-15.3. These curves were then extrapolated out to $H = 19.1$ (i.e., $D = 1$ km for $p_v = 0.04$), with the mean and standard deviation values computed.

Our results suggest there were initially $(1.36 \pm 0.3) \times 10^5$ objects with $D > 1$ km in the BAF. Fig. 2 of the main text shows our results in the form of an extrapolated SFD. Note that we slightly favor the high end of this estimate, mainly because the systematic errors in H values described above would likely skew our results toward steeper slopes and higher numbers of kilometer-sized bodies.

5 Example Yarkovsky Evolution Runs

As described in the main text, we determined the fraction of material lost from the BAF through the J7:2/M5:9 resonance by tracking the dynamical evolution of test BAF members. We did this using the symplectic integration code SWIFT-RMVS3 (Levison et al. 1994) modified to accommodate Yarkovsky thermal forces (Brož 2006; see also Bottke et al. 2000). To assist readers unfamiliar with these types of computations, we present a few examples here of how these simulations work.

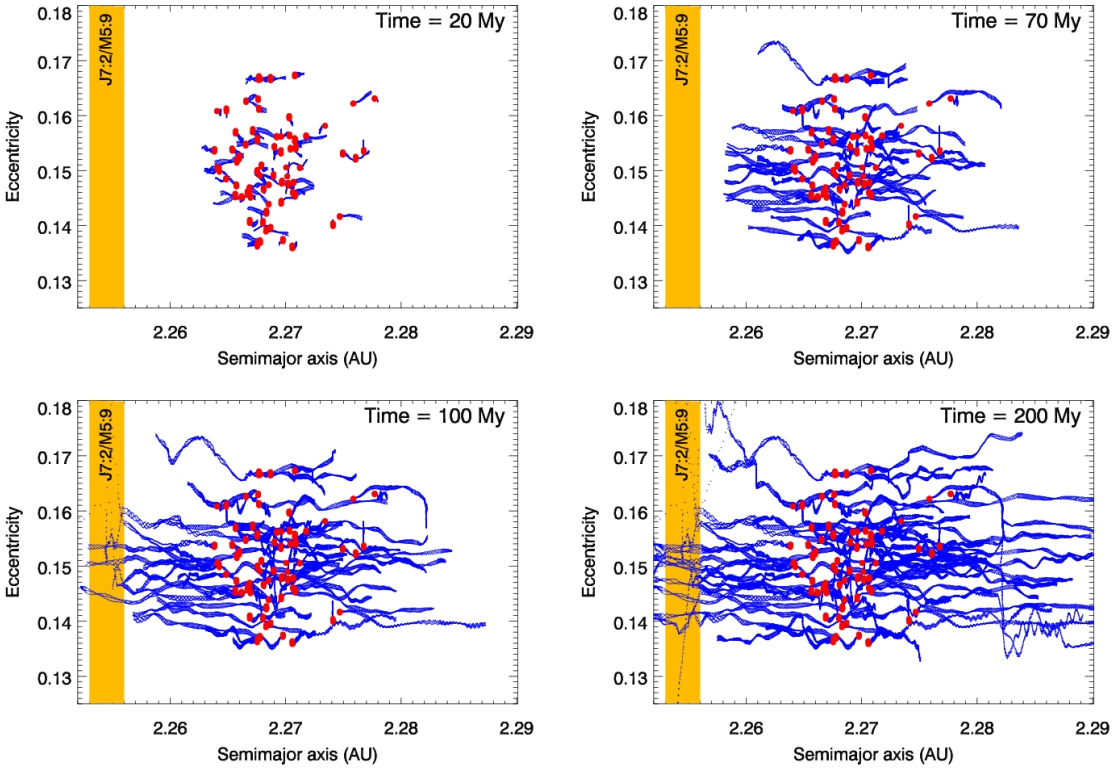

Figure S6: Dynamical evolution of 70 test asteroids with $D = 5$ km. The red dots represent the starting orbits of the bodies, which are inside the BAF. The blue lines show the orbital tracks of each body. At 100 My, a few of the bodies have reached the J7:2/M5:9 resonance, where they can get their eccentricity values pumped up to planet-crossing orbits. Other jump this resonance and continue moving inward.

Fig. S6 shows the evolution of 70 $D = 5$ km asteroids from orbits near the J7:2/M5:9. The test asteroids were given bulk densities of 1.3 g cm^{-3}, spin periods of 6 h, random spin axis orientations, and a thermal inertia of 100 J m^{-2} s$^{-0.5}$K^{-1}. The planets Venus-Neptune were included in our integrations. Snapshots are shown at timesteps of 20, 70, 100, and 200 My. The long-term mean orbital elements of each asteroid are plotted in this figure. These values were calculated by (i) grouping the orbital elements of each asteroid within a 10 My window, (ii) computing their average, and (iii) shifting the 10 My window by 0.1 My and repeating the process (see also Nesvorný et al. 2002). While we find this procedure simple and reasonable accurate for many purposes, it is important to note that averaged elements are not the same as full-fledged synthetic proper elements (e.g., Knežević et al. 2002). Proper elements are designed to eliminate the effects of planetary perturbations that can cause an asteroid's e and i values to oscillate over short time scales. In an ideal situation, where dynamical chaos does not take place and where non-gravitational forces (such at the Yarkovsky effect) play no role, the proper orbital elements of an asteroid are constant. If needed, these elements can be computed, but the procedure is somewhat arduous.

Yarkovsky thermal forces are shown to slowly drive the test asteroids both inward and outward in semimajor axis. Along the way, these objects pass through numerous tiny resonances where resonant jumping/trapping events produce modest changes in eccentricity. Eventually, objects evolving inward encounter the J7:2/M5:9 resonance. Some remain trapped in the resonance long enough to be pushed

onto planet-crossing orbits, where they go on to strike the Sun, a planet, or are ejected from the inner solar system by a close encounter with Jupiter. Others jump the resonance and continue evolving inward.

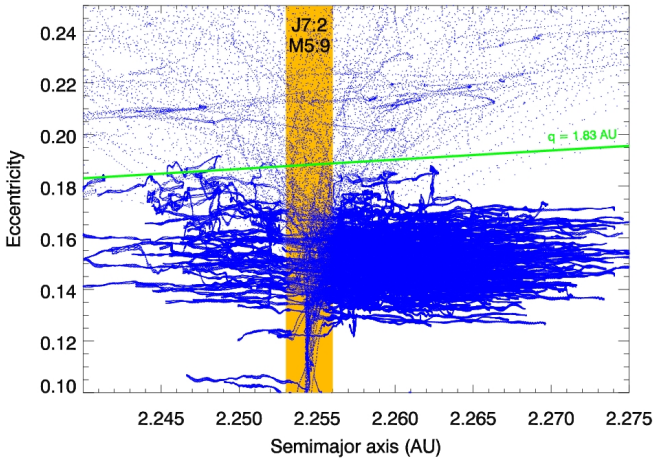

Figure S7: The dynamical evolution of $D = 10$ km test asteroids in the BAF by the Yarkovsky effect. The green line shows perihelion distance $q = 1.83$ AU in our averaged orbital elements where these objects first encounter Mars. Note that if were plotting osculating orbital elements rather than orbital elements averaged over a 10 My window, the osculating perihelion distance needed to cross Mars's orbit is $q = 1.67$ AU.

Fig. S7 shows the evolution of 750 test asteroids in the BAF with $D = 10$ km, with orbital elements averaged as described above. Here we took the largest 750 red objects with $a > a_{\rm bap}$ found in Fig. 1 (main text) and gave them starting $a_{\rm start}$ values of $a_{\rm bap} - (a - a_{\rm bap})/2$. The objects were numerically tracked for 200 My. We then determined the fraction of objects that become trapped in the J7:2/M5:9 long enough to reach Mars-crossing orbits.

6 Planetary Impact Rates From Test Objects Placed In J7:2/M5:9

Fig. S8 shows a histogram of the impact rate of BAF members on the terrestrial planets from 9024 test bodies placed inside the J7:2/M5:9. Our runs used SWIFT-RMVS3 (Levison et al. 1994) and included gravitational perturbations from the planets Venus through Neptune. We did not include the Yarkovsky effect here because planet-crossing asteroids experience far larger orbital changes from planetary encounters and inner solar system resonances than from thermal forces.

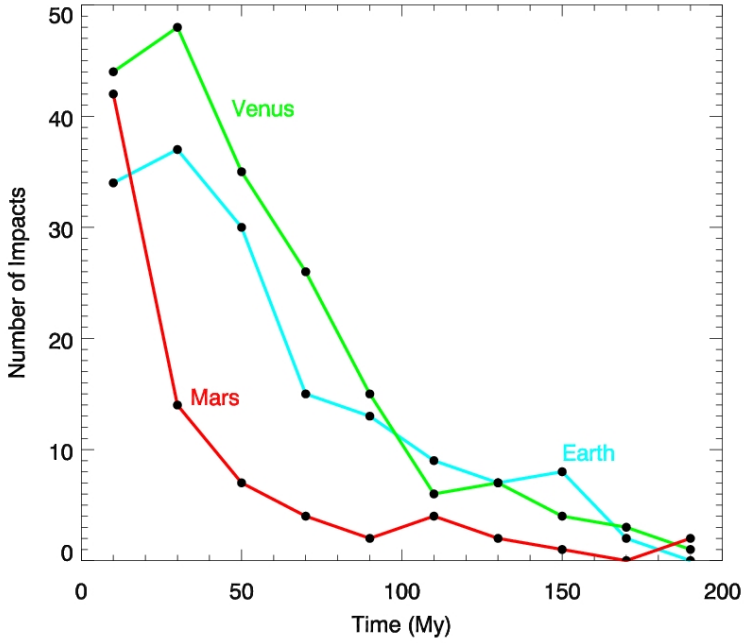

Figure S 8: Impact rate of test bodies on Venus, Earth, and Mars for objects initially injected into J7:2/M5:9 resonance in the main belt. Tracking the evolution of 9024 test bodies throughout the inner solar system, we found that 2.1%, 1.7%, and 0.9% hit Venus, Earth, and Mars over 160 My of evolution. The histogram uses bin sizes of 20 My. Note the steep drop off for Mars impactors.

These data were combined with our Yarkovsky evolution modeling work on $D = 1$ km, $D = 5$ km, and $D = 10$ km BAF members (see above and main text) to create Fig. 3 in the main text (see following section for procedure). By itself, the impact timing shown in Fig. S8 is most applicable to large BAF members ($D \gtrsim 15$ km) that, by chance, were directly injected into the J7:2/M5:9 by the Baptistina family-forming event. Accordingly, we infer that the largest BAF projectiles probably hit Mars within a few tens of My after the BAF was created 160^{+30}_{-20} My ago.

As an aside, this plot also helps demonstrate why an asteroid shower is much more likely to produce a prolonged surge in the terrestrial planet impact flux than a comet shower. Objects that reach Jupiter-crossing orbits are typically ejected out of the Solar System over relatively short timescales (~ 0.1 My; Levison and Duncan 1994). This makes it difficult for outer Solar System sources of small bodies to create and sustain sharp increases in the Earth-crossing object population. At best, perturbations to the Oort cloud from passing stars and the like can only maintain comet showers for a few My at best. Asteroids reaching $a < 2$ AU orbits, on the other hand, only cross the orbits of terrestrial planets, such that the timescales to clear these objects out of the inner Solar System are on the order of 10-100 My (e.g., Bottke et al. 2002a). This essential difference leads one to look to asteroids as the source of long-lasting shower activity.

7 Determining Number of Planetary Impacts Produced by Baptistina Family Members Using A Monte Carlo Code

7.1 Description of our Monte Carlo Code

The planetary impact flux produced by BAF fragments, which is shown in Fig. 4 of the main text, was computed by combining the following components together in a Monte Carlo code:

- The number of BAF fragments created by the family-forming event (N_0) and how this number varies with time in response to collisional evolution (see below). The BAF size distribution shown in Fig. 2 of the main text indicates N_0 for $D > 1$ km, $D > 5$ km, and $D > 10$ km at $t = 0$ My is 1.36×10^5, 1950, and 300, respectively.
- The probability distribution for BAF members of diameter D or larger to reach the J7:2/M5:9 resonance at time t after the BAF formation event ($p_1(t, D)$).
- The probability distribution for BAF fragments to hit a given planet at time t after reaching and being trapped by the J7:2/M5:9 resonance ($p_2(t)$).

For the two probability distributions, we also introduced the integrated probabilities $P_1(D) = \int_0^{160} dt\, p_1(t; D)$ and $P_2 = \int_0^{160} dt\, p_2(t)$, where t is in My. The upper integration limit corresponds to the estimated age of the BAF, which we assume is 160 My old.

To quantify these values, we used a variety of numerical methods.

- Tracking test BAF members in a numerical integration code that included the Yarkovsky effect yielded the following values: $P_1(D = 1\,\mathrm{km}) = 0.13$, $P_1(D = 5\,\mathrm{km}) = 0.23$ and $P_1(D = 10\,\mathrm{km}) = 0.19$ (see main text and Sec. 3 here for details). The flux of $D = 1$ km, 5 km and 10 km bodies entering the J7:2/M5:9 was found to be time-variable. For $D = 5$ and 10 km objects, approximately 3 times more bodies reach the J7:2/M5:9 within the first 50 My than afterwards. For $D = 1$ km bodies, the flux changed more slowly, with 50% more reaching the J7:2/M5:9 during the first 70 My than afterwards.
- The population of BAF fragments with $D > 1$ km decreases with time as family members undergo collisional evolution with both themselves and background main belt objects (see main text for details). This depletion was input into the Monte Carlo code by multiplying the $D > 1$ km results from the previous step by the function $F(t)$, defined as the ratio between the number of $D > 1$ km objects at time t after the BAF formation event and the initial number of $D > 1$ km objects (Fig. S9). Note that larger objects undergo little collisional evolution, such that $F(t)$ for $D > 5$ km and $D > 10$ km objects is ≈ 1 over 160 My.

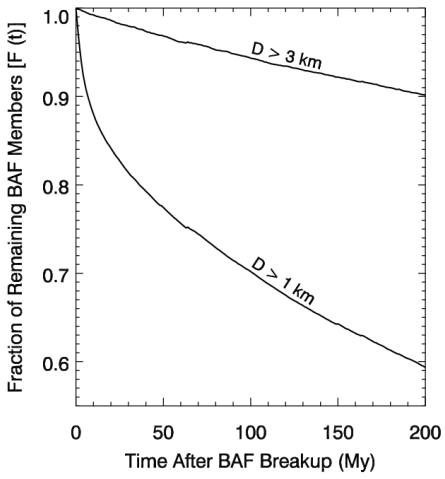

Figure S9: This plot shows $F(t)$, the ratio of BAF members with $D > 1$ km and $D > 3$ km at different times relative to the starting BAF population. The population drops off precipitously for the first 50 My and then slows as the family SFD reaches a quasi-equilibrium.

- We also followed the evolution of test objects from the J7:2/M5:9 resonance in the main belt all the way to the terrestrial planet region (see main text). This yielded $P_2 = 0.017$ for the Earth, $P_2 = 0.021$ for Venus and $P_2 = 0.009$ for Mars. The profile of $p_2(t)$ is shown in Fig. S8 of the Supplemental Discussion.

Using our Monte Carlo code, we tracked how many objects in our initial population N_0 went from their starting orbits all the way to striking the terrestrial planets. The timestep was set to a small fraction of the length of our simulation ($\Delta t \simeq 1$ My). At each timestep, we compared a random deviate to the probabilities $[p_1(t; D)\,\Delta t]$ (odds of reaching and trapped inside the J7:2/M5:9) and $[p_2(t)\,\Delta t]$ (odds that a body within the J7:2/M5:9 will hit a planet). In each simulation, we recorded the number of planetary impacts produced by our starting population and repeated the process (typically 500, 000 times). As output, the code produced a normalized distribution of planetary impacts (Fig. S10).

7.2 Results

Earth impacts. We predict that the number of $D > 1$ km projectiles striking Earth from the BAF over 160 My was 200 ± 60. It is interesting to note that this number is smaller than the zero-order estimation ($N_0 \times P_1(D = 1\,\mathrm{km}) \times P_2$) because the two probabilistic processes are *not* independent but consequential ("Component 2 only happens after component 1"). Hence, it is important to use a Monte Carlo code formulated as described above. Using the code again with $N_0 = 1950$, we found the number of $D > 5$ km BAF projectiles that hit Earth was 6 ± 2.

For K/T-sized projectiles from the BAF ($D > 10$ km), the number striking the Earth can be 0, 1, or a few. The $D > 10$ km panel of Fig. S10 shows our results. Overall, there is a $\sim 40\%$ likelihood that no K/T impact will come from the BAF and a $\sim 60\%$ likelihood of having one or more impacts.

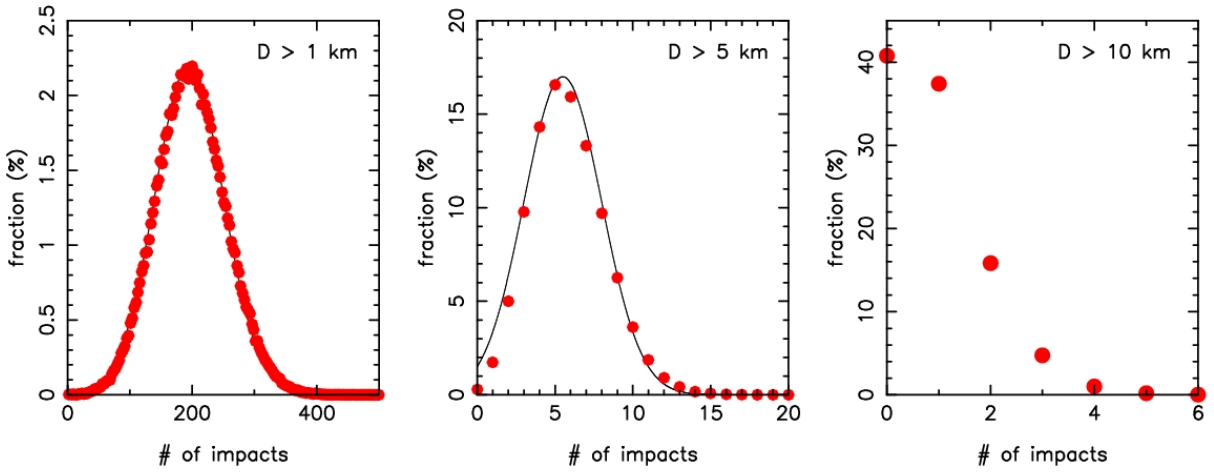

Figure S 10: Probability distribution of expected Earth impacts from BAF fragments within the last 160 My (red symbols). Three impactor sizes are considered: $D > 1, D > 5$, and $D > 10$ km. The solid black lines show Gaussian approximations of each distribution. For $D > 1$ km, we find a median value of 200 impacts and a standard deviation of 60. For $D > 5$ km, the median value is 6 impacts with a standard deviation of ~ 2. For $D > 10$ km, the number of impacts is too small to be approximated by a Gaussian distribution.

Venus impacts. The crater record on Venus is more complete in large craters for its age than that of the Earth (Herrick et al. 1997), with 4 craters produced by $D \gtrsim 10$ km projectiles over the last 730 My (Korycansky and Zahnle 2005). To investigate this population, we used a variant of the Monte Carlo code describe above. We assumed that Venus was bombarded by a background impactor population of $D \gtrsim 10$ km projectiles between 0-730 Ma, with the average interval between impacts being one per 350 My (similar to that derived for the Earth; see main text). The relatively small contribution of impactors from the long period comet population was neglected (see following section). Superposed on this was the BAF asteroid shower, which we assumed started 160 Ma. At the end of each simulation, we checked to see if 4 K/T impacts were produced. If so, we recorded how many craters were made by background and BAF projectiles. Approximately 83,000 of our 500,000 Monte Carlo simulations (one-sixth of our runs) met this criteria.

Figure S11 shows the probability of each background/BAF combination taking place. We found an 80% probability that the BAF asteroid shower created at least one of the 4 largest craters on Venus, with the most likely case being 1 crater formed by the BAF and 3 by the background ($\sim$ 38%). The probability that BAF fragments created 2 or more of the large craters was 44%.

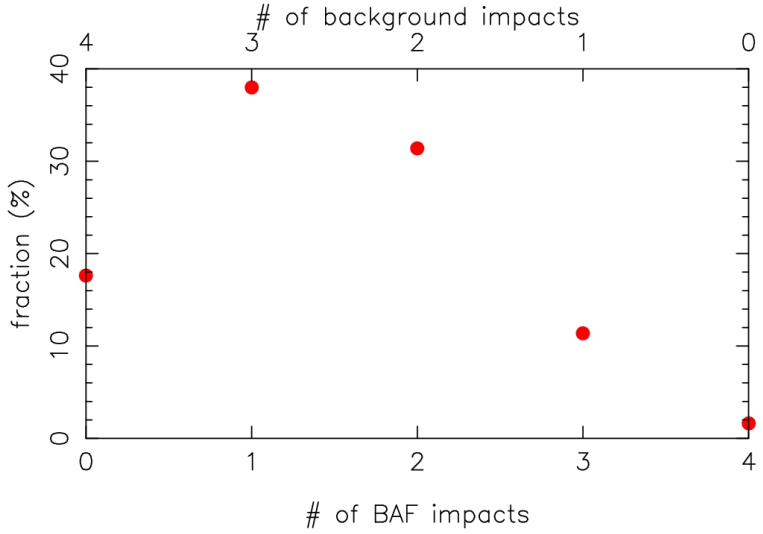

Figure S11: Probability distribution describing the likelihood that that the 4 largest craters on Venus were created by the BAF asteroid shower or background projectiles. The contribution from BAF fragments is at the bottom abscissa, while the contribution from the background population is the top abscissa. The sum in all cases is set to 4. The ordinate describes the probability of each scenario.

8 The Impact Rate of Nearly-Isotropic Comets with Earth

Some craters on the terrestrial planets have almost certainly come from the impact of nearly isotropic comets (NICs). The question is whether the NIC impact flux was high enough over the last 160 My to significantly influence the results presented in the main text. We explore this issue here by estimating the NIC impact flux with Earth and comparing those results to those of BAF projectiles.

NICs come from the Oort cloud, which is located at a distance of $a > 3000$ AU (Weissman 1996). There are two main types of NICs: (i) Long period comets (LPCs), with periods longer than 200 years and Tisserand parameter $T < 2$, and (ii) Halley-type comets (HTCs), with periods less than 200 years and $T < 2$ (Levison 1996). Both reside outside the Jupiter-family comet (JFC) region, whose contribution to the NEO population was discussed in Bottke et al. (2002b) and Stokes et al. (2003). The observed population of LPCs has nearly isotropic inclinations, while HTCs show a preference for prograde orbits (Levison et al. 2001). By definition, LPCs must have $a > 35$ AU, but most observed LPCs have $a \sim 20,000$ AU (Weissman 1996). Most of the observed HTCs, which have traditionally been considered the short-period tail of the LPCs, have $a \sim$ 10-30 AU (Weissman 1996). In either case, for NICs to reach collision orbits with the terrestrial planets, they need $e \sim 1$. Note that HTC impact rates are not explored in this section because they are thought to be considerably lower than those of the LPC population (e.g., Levison et al. 2002).

Impact probabilities. A recent estimate of the impact rate for individual LPCs on Earth was made by Francis (2005), who determined this value by modeling comet discovery statistics made by the LINEAR survey. Combining his results with the Weissman (2007) estimate of the mean impact probability of individual LPCs with the Earth (2.4×10^{-9} per comet per perihelion passage), we find that the mean interval between LPC impacts with a total absolute magnitude $H_{\rm T} < 9$ is ~ 190 My.

Conversion from magnitudes to diameters. To compare the above impact interval with the BAF impact rates described in the main text, we need to know (i) how to convert comets with $H_{\rm T} < 9$ into a diameter D and (ii) the size-frequency distribution of comets in the LPC population. There is considerable uncertainties in both components. Still, as we explain below, the properties of the JFC population, if carefully applied, may be used to glean insights into the nature of the LPC population.

Consider the following. New dynamical scenarios for the very late stages of planet formation indicate that comet reservoirs like the Kuiper belt, scattered disk, and Oort cloud may have been created ~ 3.9 Gy ago in the same event that also produced the so-called Lunar Late Heavy Bombardment (LHB). More specifically, we are referring to the so-called "Nice" model, a colloquial name for the numerical simulations described in Tsiganis et al. (2005), Morbidelli et al. (2005), and Gomes et al. (2005). They found that a plausible scenario may now exist to not only reproduce the LHB as a terminal cataclysm but also explain many other longstanding problems in Solar System dynamics.

In the Nice model, the Jovian planets were assumed to have grown on initially nearly circular, coplanar orbits with a more compact configuration than they have today (all were located between 5-15 AU). Slow planetary migration was induced in the Jovian planets by gravitational interactions with planetesimals leaking out of a $\sim 35 M_\oplus$ planetesimal disk residing between ~ 16 to ~ 30 AU. These interactions steadily stretched the system of planets over hundreds of My. Eventually, after a delay of ~ 600 My set by the initial configuration of the gas giants (Gomes et al. 2005), Jupiter and Saturn crossed their mutual 1:2 mean motion resonance, which caused their e and i values to jump from values near zero to their current values. In turn, this caused Uranus and Neptune to become unstable and be scattered outward, such that they penetrated the disk and migrated through it. The orbits of Uranus and Neptune were then circularized by dynamical friction produced by bodies in the disk.

Assuming this is true, the comet reservoirs mentioned above were produced 3.9 Gy ago by comets in the 16-30 AU range scattering off of or gravitationally interacting with the migrating Jovian planets. This means the JFCs, HTCs, and LPCs came, more or less, from the same source population. It also implies that all three comet populations experienced roughly the same degree of collisional processing. We infer from this that the size distribution and magnitude properties of the JFCs, if properly applied, can be used to tell us about the nature of the LPC population.

This takes us to the conversion of cometary magnitudes to nucleus diameters. Published estimates of the nucleus size of $H_{\rm T} = 9$ JFCs range from $D = 0.8$ km (Bailey et al. 1994) to $D = 2$ km (Weissman 1990). Using results for the JFC population from Bottke et al. (2002b), as well as the estimate that 40%

of all JFCs fade and become dormant comets (Levison et al. 2002), we predict that $H_{\rm T} = 9$ JFCs (and therefore LPCs) should correspond to a nucleus diameter of $D = 1.6$ km.

Comet size-frequency distributions. The power law slope for the LPC SFD (γ, where $N(>D) \propto D^{\gamma}$) is unknown. Estimates for γ from the JFC population, which we use as a proxy for the LPCs, are better quantified, with values ranging from -1.7 (e.g., Weissman and Lowry 2006) to -2.7 (e.g., Tancredi et al. 2006; Fernández and Morbidelli 2006). Note that Tancredi et al. (2006) claims that previous studies suffer from several problems (e.g., selection effects, etc.); in a reanalysis of previous works, they found γ values that were close to their preferred value of -2.7. On the other hand, Tóth (2006), who reviewed all the work on this topic, claims that his preferred value is -2.0.

In the end, we decided to use γ values between -2.0 and -2.7 for our computations. Support for this range of values comes from the crater SFDs found on both Ganymede and Callisto, whose $D > 20$ km craters show power law slopes between -2.0 and -3.0 (e.g., Seddio and Schenk 2007).

LPC impacts on Earth. To directly compare LPC impactors to those produced by BAF fragments, we computed the comet size capable of producing the same amount of kinetic energy upon Earth impact (E_k) as a given BAF projectile.

$$E_k = 1/2\, m_{\rm BAF} V_{\rm BAF}^2 = 1/2\, m_{\rm c} V_{\rm c}^2 \tag{9}$$

Here the masses of the BAF and LPC projectiles are $m_{\rm BAF}$ and m_c, respectively, while the impact velocities on Earth are $V_{\rm BAF} = 20$ km s^{-1} (Bottke et al. 2002b) and $V_{\rm c} = 50.5$ km s^{-1} (Weissman 2007), respectively. Solving for $D_{\rm c}$, the diameter of the LPC, we get:

$$D_{\rm c} = D_{\rm BAF} \left(\frac{\rho_{\rm BAF} V_{\rm BAF}^2}{\rho_{\rm c} V_{\rm c}^2} \right)^{1/3} \tag{10}$$

where the bulk densities of the BAF and LPC projectiles are $\rho_{\rm BAF} = 1.3$ g cm^{-3} and $\rho_{\rm c} = 0.5$ to 0.6 g cm^{-3} (e.g., Britt et al. 2006; Weissman and Lowry 2006), respectively. Accordingly, these results suggest that an LPC with $D_{\rm c} \approx 7$ km imparts the same kinetic energy on Earth as a BAF projectile with $D_{\rm BAF} = 10$ km.

We now have all of the information needed to compute the impact interval for LPCs of different sizes (I) and compare those results to BAF projectiles. For I, we get:

$$I({\rm My}) = 190\,{\rm My} \left(\frac{D_{\rm c}}{1.6\,{\rm km}} \right)^{\gamma} \tag{11}$$

Assuming $\gamma = -2.0$ to -2.7, we find the LPCs corresponding to the same impact energies as $D_{\rm BAF} > 1$ km projectiles strike the Earth once every 20-40 My. In contrast, we showed in the main text that km-sized BAF and background projectiles have hit the Earth > 400 times over the last 160 My. We infer from this that LPCs can be neglected for our $D > 1$ km impact statistics.

For LPCs that strike the Moon with the same kinetic energy as Tycho-sized impactors from the BAF (i.e., $D_{\rm BAF} > 4$ km), the interval between lunar impacts is extremely small (11,500-17,000 My; recall that the Moon has a gravitational cross section that is only $\sim 5\%$ that of the Earth). These low rates mean that LPCs have little effect on the Tycho impact probability values presented in the main text.

Finally, for impactors with the same kinetic energy as a K/T-sized impactor from the BAF (i.e., $D_{\rm BAF} > 10$ km), we infer that the interval between impacts on Earth is 3,800-11,000 My. These values are small but still significant enough to modify the K/T impact probability calculation presented in the main text by a few percent (i.e., the probability that the K/T impact came from BAF fragments vs. primitive background objects).

References

Bailey, M. E., Clube, S. V. M., Hahn, G., Napier, W. M., Valsecchi, G. B. 1994. Hazards due to giant comets: Climate and short-term catastrophism. In *Hazards Due to Comets and Asteroids* (T. Gehrels, M. S. Matthews, Eds.), pp. 479-533 (University of Arizona Press, Tucson).

Bendjoya, P., and Zappalà, V., 2002. Asteroid family identification. In *Asteroids III* (W.F. Bottke, A. Cellino. P. Paolicchi and R.P. Binzel, Eds.), pp. 613–618. (University of Arizona Press, Tucson).

Bogard, D. 1995. Impact ages of meteorites: A synthesis. *Meteoritics* **30**, 244-269.

Bottke, W. F., Rubincam D. P., and Burns, J. A. 2000. Dynamical evolution of main belt meteoroids: Numerical simulations incorporating planetary perturbations and Yarkovsky thermal forces. *Icarus* **145**, 301–331

Bottke, W.F., Vokrouhlický, D., Rubincam, D.P., and Brož, M., 2002a. Dynamical evolution of asteroids and meteoroids using the Yarkovsky effect. In *Asteroids III* (W.F. Bottke, A. Cellino. P. Paolicchi and R.P. Binzel, Eds.), pp. 395–408. (University of Arizona Press, Tucson).

Bottke, W. F., Morbidelli, A., Jedicke, R., Petit, J.-M., Levison, H. F., Michel, P., Metcalfe, T. S. 2002b. Debiased orbital and absolute magnitude distribution of the near-Earth objects. *Icarus* **156**, 399-433.

Bottke, W. F., Durda, D., Nesvorny, D., Jedicke, R., Morbidelli, A., Vokrouhlický, D., and Levison., H. 2005. The origin and evolution of stony meteorites. In *Dynamics of Populations of Planetary Systems* (eds. Knezevic, Z. and Milani, A.) IAU Colloquium 197, Belgrade, 357-376. Cambridge Univ. Press.

Bottke, W. F., Nesvorný, D., Grimm, R. E., Morbidelli, A., O'Brien, D. P. 2006a. Iron meteorites as remnants of planetesimals formed in the terrestrial planet region. *Nature* **439**, 821–824.

Bottke, W.F., Vokrouhlický, D., Rubincam, D.P., Nesvorný, D., 2006b. The Yarkovsky and YORP effects: Implications for asteroid dynamics. *Ann. Rev. Earth Planet. Sci.* **34**, 157–191.

Britt, D. T., Consolmagno, G. J., Merline, W. J. 2006. Small body density and porosity: New data, new insights. *LPSC* **37**, 2214.

Burbine, T. H., McCoy, T. J., Meibom, A., Gladman, B., and Keil K. 2002. Meteoritic parent bodies: Their number and identification. In *Asteroids III* (W.F. Bottke, A. Cellino. P. Paolicchi and R.P. Binzel, Eds.), pp. 653–667 (University of Arizona Press, Tucson).

Bus, S. J., Vilas, F., and Barucci, M. A. 2002. Visible wavelength spectroscopy of asteroids. In *Asteroids III* (W.F. Bottke, A. Cellino. P. Paolicchi and R.P. Binzel, Eds.), pp. 169–182 (University of Arizona Press, Tucson).

Čapek, D. and Vokrouhlický, D. 2004. The YORP effect with finite thermal conductivity. *Icarus* **172**, 526–536.

Carruba, V., Michtchenko, T. A., Roig, F., Ferraz-Mello, S. & Nesvorný, D. 2005. On the V-type asteroids outside the Vesta family. I. Interplay of nonlinear secular resonances and the Yarkovsky effect: the cases of 956 Elisa and 809 Lundia, *Astron. Astrophys.* **441**, 819–829.

Delbó, M., Dell'Oro, A., Harris, A. W., Mottola, S., and Mueller, M. 2007. Thermal inertia of near-Earth Asteroids and strength of the Yarkovsky effect. *Icarus*, in press.

Farinella, P., Vokrouhlický, D., Hartmann, W. K., 1998. Meteorite delivery via Yarkovsky orbital drift. *Icarus* **132**, 378–387.

Fernández, J. A., Morbidelli, A. 2006. The population of faint Jupiter family comets near the Earth. *Icarus* **185**, 211-222.

Fowler, J.W. and Chillemi, J. R. 1992. IRAS asteroid data processing. In *The IRAS Minor Planet Survey* (E.F. Tedesco, ed) Tech. Report PL-TR-92-2049., Phillips Laboratory, Hanscom Air Force Base, Massachusetts, pp 17-43.

Francis, P. J. 2005. The demographics of long-period comets. *Astrophys. J.* **635**, 1348-1361.

Gladman, B. J., Migliorini, F., Morbidelli, A., Zappala, V., Michel, P., Cellino, A., Froeschle, C., Levison, H. F., Bailey, M., Duncan, M. 1997. Dynamical lifetimes of objects injected into asteroid belt resonances. *Science* **277**, 197–201.

Gomes, R., Levison, H. F., Tsiganis, K., Morbidelli, A. 2005. Origin of the cataclysmic late heavy bombardment period of the terrestrial planets. *Nature* **435**, 466-469.

Herrick, R. R. Sharpton, V. L., Malin, M. C., Lyons, S. N., and Feely, K. 1997. Morphology and morphometry of impact craters. In *Venus II* (Bougher, S. W. et al., Eds), pp. 1015–1046 (University of Arizona Press, Tucson).

Ivezić, Ž., and 32 colleagues 2001. Solar System Objects Observed in the Sloan Digital Sky Survey Commissioning Data. *Astron. J.* **122**, 2749–2784.

Jedicke, R., J. Larsen, and T. Spahr. 2002. Observational selection effects in asteroid surveys. In *Asteroids III* (W.F. Bottke, A. Cellino. P. Paolicchi and R.P. Binzel, Eds.), pp. 71–88. (University of Arizona Press, Tucson).

Knežević, Z., A. Lemaître, and A. Milani. 2002. The determination of asteroid proper elements. In *Asteroids III* (W.F. Bottke, A. Cellino. P. Paolicchi and R.P. Binzel, Eds.), pp. 603–612. (University of Arizona Press, Tucson).

Knežević, Z., and Milani, A. 2003. Proper element catalogs and asteroid families. *Astron. Astrophys.* **403**, 1165-1173. See also Milani, A. *et al.* The Asteroid-Dynamics Site (AstDyS). http://newton.dm.unipi.it/

Korycansky, D. G., and Zahnle, K. J. 2005. Modeling crater populations on Venus and Titan. *Planet. Space Sci.* **53**, 695–710.

Levison, H. F. and M. J. Duncan 1994. The long-term dynamical behavior of short-period comets. *Icarus* **108**, 18-36.

Levison, H. F. 1996. Comet taxonomy. *ASP Conf. Ser. 107: Completing the Inventory of the Solar System*, 173-191.

Levison, H. F., Dones, L., Duncan, M. J. 2001. The origin of Halley-type comets: Probing the inner Oort cloud. *Astron. J.* **121**, 2253-2267.

Levison, H. F., Morbidelli, A., Dones, L., Jedicke, R., Wiegert, P. A., Bottke, W. F. 2002. The mass disruption of Oort cloud comets. *Science* **296**, 2212-2215.

Marzari, F., Cellino, A., Davis, D. R., Farinella, P., Zappala, V., and Vanzani, V. 1996. Origin and evolution of the Vesta asteroid family. *Astron. Astrophys.* **316**, 248–262.

Morbidelli, A. and D. Nesvorný 1999. Numerous weak resonances drive asteroids toward terrestrial planets orbits. *Icarus* **139**, 295-308.

Morbidelli, A., Levison, H. F., Tsiganis, K., Gomes, R. 2005. Chaotic capture of Jupiter's Trojan asteroids in the early Solar System. *Nature* **435**, 462-465.

Mothé-Diniz, T., Roig, F., Carvano, J. M. 2005. Reanalysis of asteroid families structure through visible spectroscopy. *Icarus* **174**, 54-80.

Nesvorný, D., Bottke, W. F., Dones, L., and Levison, H. F., 2002. The recent breakup of an asteroid in the main-belt region. *Nature* **417**, 720–722.

Nesvorný, D., Bottke, W. F., Levison, H. F., Dones, L., 2003. Recent origin of the Solar System dust bands. *Astrophys. J.* **591**, 486–497.

Nesvorný, D., and Bottke, W. F. 2004. Detection of the Yarkovsky effect for main-belt asteroids. *Icarus* **170**, 324–342.

Nesvorný, D., and Vokrouhlický, D. 2006. New candidates for recent asteroid breakups, *Astron. J.* **132**, 1950–1958.

Nesvorný, D., Vokrouhlický, D., and Bottke, W. F. 2006. A main belt asteroid break-up 450 ky ago. *Science* **312**, 1490-1490.

Nesvorný, D., Vokrouhlický, D., Bottke, W. F., Gladman, B., and Haggstrom, T. 2007. Express delivery of fossil meteorites from the inner asteroid belt to Sweden. *Icarus*, in press.

Pravec, P., and A. W. Harris. 2007. Binary asteroid population: 1. Angular momentum content. *Icarus*, in press.

Seddio, S., Schenk, P. 2007. Crater Densities, Surface Ages and Evolution of Ganymede's Bright Terrain. *LPSC* **38**, 2350.

Stokes, G., D. Yeomans, W.F. Bottke, S. Chesley, J. B. Evans, R. E. Gold, A. W. Harris, D. Jewitt, T.S. Kelso, R. McMillian, T. Spahr, S. P. Worden. 2003. A Study to Determine the Feasibility of Extending the Search for Near Earth Objects to Smaller Limiting Magnitudes. *Report Prepared at the Request of NASA Headquarters Office of Space Science's Solar System Exploration Division.* Full 166-page report available as a PDF document at: neo.jpl.nasa.gov/neo/report.html

Stuart, J. S. 2006. Photometric Calibration of LINEAR and NEA Population Statistics. *IAU Symposium 236*, Prague, Czech Republic.

Tancredi, G., Fernández, J. A., Rickman, H., Licandro, J. 2006. Nuclear magnitudes and the size distribution of Jupiter family comets. *Icarus* **182**, 527-549.

Tedesco, E. F., Noah, P. V., Noah, M., Price, S. D. 2002. The supplemental IRAS minor planet survey. *Astron J.* **123**, 1056–1085.

Tóth, I. 2006. Connections between asteroids and cometary nuclei. In *Asteroids Comets, Meteors 2005* **IAU Symp. 229** (S. Ferraz-Mello, D. Lazzaro and J.A. Fernández, Eds), pp. 67-96. (Cambridge Univ. Press, Cambridge).

Tsiganis, K., Gomes, R., Morbidelli, A., Levison, H. F. 2005. Origin of the orbital architecture of the giant planets of the Solar System. *Nature* **435**, 459-461.

Vokrouhlický, D., 1998. Diurnal Yarkovsky effect as a source of mobility of meter-sized asteroidal fragments. I. Linear theory. *Astron. Astrophys.* **335**, 1093–1100.

Vokrouhlický, D., 1999. A complete linear model for the Yarkovsky thermal force on spherical asteroid fragments. *Astron. Astrophys.* **344**, 362–366.

Vokrouhlický, D., Čapek, D., 2002. YORP-induced long-term evolution of the spin state of small asteroids and meteoroids. Rubincam's approximation. *Icarus* **159**, 449–467.

Vokrouhlický, D., Brož, M., Bottke, W. F., Nesvorný, D., Morbidelli, A. 2006a. Yarkovsky/YORP chronology of asteroid families. *Icarus* **182**, 118–142.

Vokrouhlický, D., Brož, M., Morbidelli, A., Bottke, W. F., Nesvorný, D., Lazzaro, D., Rivkin, A. S. 2006b. Yarkovsky footprints in the Eos family. *Icarus* **182**, 92–117.

Vokrouhlický, D., Brož, M., Bottke, W. F., Nesvorný, D., Morbidelli, A. 2006c. The peculiar case of the Agnia asteroid family. *Icarus* **183**, 349–361.

Weissman, P. R. 1990. The Oort cloud. *Nature* **344**, 825-830

Weissman, P. R. 1996. The Oort Cloud. In *Completing the Inventory of the Solar System* (T. W. Rettig and J. M. Hahn, Eds) **ASP Conf. Ser. 107** pp. 265-288 (Astron. Soc. Pacific, San Francisco).

Weissman, P. R. 2007. The cometary impactor flux at the Earth. In *Near Earth Objects, Our Celestial Neighbors: Opportunity and Risk* (A. Milani, G. B. Valsecchi, and D. Vokrouhlický, Eds), pp. 441-450. (Cambridge Univ. Press, Cambridge).

Weissman, P. R., and Lowry, S. C. 2006. Size Distribution, structure and density of cometary nuclei. In *Spacecraft reconnaissance of asteroid and comet interiors.* LPI Contribution 1325, 76-77.

Zappalà, V., Cellino, A., Farinella, P., Knežević, Z. 1990, Asteroid families. I. Identification by hierarchical clustering and reliability assessment. *Astron. J.* **100**, 2030–2046.